Available online at www.sciencedirect.com
SCIENCE DIRECT
Vision Research 45 (2005) 3432–3444
Vision Research
www.elsevier.com/locate/visres

Three-dimensional adaptive optics ultrahigh-resolution optical coherence tomography using a liquid crystal spatial light modulator

Enrique J. Fernández [a,b], Boris Považay [a], Boris Hermann [a], Angelika Unterhuber [a], Harald Sattmann [a], Pedro M. Prieto [b], Rainer Leitgeb [a], Peter Ahnelt [c], Pablo Artal [b], Wolfgang Drexler [a,*]

[a] Center for Biomedical Engineering and Physics, Vienna University of Medicine, Austria
[b] Laboratorio de Optica, Universidad de Murcia, Spain
[c] Center for Physiology and Pathophysiology, Vienna University of Medicine, Austria

Received 3 June 2005; received in revised form 29 August 2005

Abstract

A liquid crystal programmable phase modulator (PPM) is used as correcting device in an adaptive optics system for three-dimensional ultrahigh-resolution optical coherence tomography (UHR OCT). The feasibility of the PPM to correct high order aberrations even when using polychromatic light is studied, showing potential for future clinical use. Volumetric UHR OCT of the living retina, obtained with up 25,000 A-scans/s and high resolution enables visualization of retinal features that might correspond to groups of terminal bars of photoreceptors at the external limiting membrane.

Keywords: Adaptive optics; Optical coherence tomography; Three-dimensional retinal imaging; Photoreceptors

1. Introduction

Ultrahigh-resolution optical coherence tomography (UHR OCT) is an imaging modality (Drexler et al., 1999) based on low coherence interferometry employing ultrabroad bandwidth light sources (Drexler, 2004). OCT can be understood as an indirect measurement of the time of flight and intensity of the light back-scattered from the sample (Huang et al., 1991). This is fundamentally performed by using a low coherence light source and a Michelson interferometer (Swanson et al., 1993), similarly to white light interferometry. OCT is a very attractive tool for medical diagnostics mainly due to both its high resolution and its non-invasive character. This technique has permitted non-invasive imaging of the retina and cornea morphology in vivo with unprecedented axial resolution (Drexler et al., 2001). UHR OCT allows resolving all major intraretinal layers in the living human eye, enabling the study, and early diagnosis of retinal pathologies (Drexler et al., 2003; Ko et al., 2004).

It is well known that in low coherence interferometry the axial and the transversal resolution are decoupled. The former is governed by the spectral bandwidth of the source, while the latter is primarily limited by the numerical aperture and imaging quality of the system. In case of ophthalmic UHR OCT, where the eye constitutes the effective objective of the system, up to 2–3-μm of axial resolution has been demonstrated, with transversal resolutions in the order of 20-μm. This transversal resolution is relatively modest in respect to the axial one. For 3-D OCT imaging of cellular retinal features, e.g., photoreceptors, ganglion

* Corresponding author. Tel.: +43 1 4277 60726.
E-mail address: Wolfgang.Drexler@meduniwien.ac.at (W. Drexler).

0042-6989/$ - see front matter © 2005 Elsevier Ltd. All rights reserved.
doi:10.1016/j.visres.2005.08.028

or retinal pigment epithelium cells, with transverse dimensions in the range of 10 μm, isotropic resolution would be extremely advantageous.

Most of the ophthalmic OCT systems employ a beam of about 1–2-mm diameter to illuminate the retina. A possible approach to increase transversal resolution in OCT tomograms, therefore producing a smaller spot of light on the retina, is the expansion of the beam and pupil, enlarging the effective numerical aperture of the eye. Nevertheless, ocular aberrations in pupils larger than 1.5–2-mm diameter notably degrade retinal images (Castejón-Mochón, López-Gil, Benito, & Artal, 2002; Porter, Guirao, Cox, & Williams, 2001; Thibos, Hong, Bradley, & Cheng, 2002). Hence, the expansion of beam and pupil diameter is not reasonable unless aberrations are simultaneously corrected. In this context, adaptive optics (AO) has been demonstrated in the human eye, measuring and correcting the ocular aberrations in real time (Fernández, Iglesias, & Artal, 2001; Hofer et al., 2001a). AO has been successfully applied in scanning laser ophthalmoscopy (Roorda et al., 2002) and flood illumination cameras (Hofer et al., 2001a), notably increasing the resolution and contrast of these imaging techniques, enabling the detection of individual photoreceptors in the living retina. First attempts in combining a coherence-gated camera with AO for en face OCT imaging with standard axial resolution (15–20 μm) has been reported (Miller, Qu, Jonnal, & Thorn, 2003). The successful combination of AO with UHR OCT has recently been demonstrated (Hermann et al., 2004), where high axial (3 μm) and improved transversal (~5–10 μm) resolution two-dimensional (B-scan) imaging has been achieved. In this work, a beam of 3.68 mm diameter was used, correcting ocular aberrations before acquiring retinal OCT images. The benefits of combining AO with UHR OCT were signal-to-noise ratio and transversal resolution improvement of the retinal OCT tomograms. Nevertheless, the reported approach suffered of several limitations: on one hand the performance of the correcting device was limited. A membrane deformable mirror with 37 independent electrodes was used, with a stroke insufficient to perform perfect aberration correction, even in normal eyes with moderate pupil sizes (Fernández & Artal, 2003). On the other hand, time-domain OCT, being relatively slow, was employed. In this modality, a translation of the reference arm for depth scanning is required on the subject's retina at every point, therefore preventing high sampling speeds in a reasonable time. The effect of the eye's movements, as regular saccades, is highly noticeable in these images, making the use of sophisticated post-processing techniques necessary, even in a single B-scan. Hence, 3-D in vivo imaging is difficult to accomplish with time-domain systems.

As an alternative approach, frequency-domain OCT, also referred to as Fourier Domain OCT or Spectral Domain OCT in literature (Fercher, Hitzenberger, Kamp, & El-Zaiat, 1995) allows the retrieval of tomograms without necessity of a moving mirror in the reference arm for depth scanning, allowing higher sampling speeds and signal to noise ratios compared to the original OCT technique, called time-domain OCT (Cense et al., 2004; Leitgeb et al., 2004; Wojtkowski et al., 2004). This enables the acquisition of B-scans with high transverse sampling almost free of artifacts associated to eye movements, and allows the recording of 3-D tomograms within in a short time. In this technique, the detection of interferences between the light coming from the sample and reference arm is performed through recording the optical spectrum, which is spatially distributed by means of a dispersive element onto the detector. First attempts to combine AO and frequency-domain OCT for 2-D retinal imaging has recently been reported (Zhang, Rha, Jonnal, & Miller, 2005).

Regarding the AO correcting device, a liquid crystal programmable phase modulator (LC-PPM) has recently been demonstrated as a capable correcting device for ocular aberrations in monochromatic light (Prieto, Fernández, Manzanera, & Artal, 2004). As a phase modulator capable of phase wrapping, the PPM is not limited by physical stroke like deformable mirrors are in monochromatic light. The spatial resolution, i.e., the capability for producing or correcting aberrations with high spatial frequencies, is also several orders of magnitude larger than in other correcting devices, because the number of independent pixels, up to 6,00,000.

In the current work, we are studying and demonstrating the feasibility of the use of a liquid crystal programmable phase modulator as correcting device with polychromatic light, in combination with frequency-domain UHR OCT for 3-D retinal imaging.

2. Experimental apparatus

In the PPM (Hamamatsu, X7550) a parallel-aligned liquid crystal layer is sandwiched between two transparent electrodes. An internal display generates the image, which optically drives the orientation of the molecules of the liquid crystal layer (Li et al., 1998). The images generated on the internal display, which for this particular model allows up to VGA resolution, meaning 2,30,400 independent pixels and 8-bit depth, are directly addressable by the control computer, similar to a standard LCD. The internal image is projected optically on a photoresistive layer, locally changing the impedance of the material. Pixilation effects from the internal display are removed from the projected images, making the device virtually free from diffraction effects associated to pixilation. The photoresistive layer also optically isolates the internal display and the liquid crystal layer. The variations of impedance induced on the photoresistive material locally modify the electrical field between the two transparent electrodes, inducing different orientations on the molecules of the liquid crystal layer. It is precisely the orientation of the molecules that determines the refractive index of the liquid crystal screen, therefore enabling the local modulation of phase. Only the phase corresponding to component of the light parallel to the initial alignment of the molecules of the liquid crystal is

affected. Consequently, the use of linear polarized light is mandatory with the PPM.

The experimental apparatus was divided into two different parts: the frequency-domain interferometer and the AO system. Both systems were connected by optical fibers. Fig. 1 schematically shows the entire set-up. The illumination source in the system for testing the PPM was a compact, prismless, mode-locked Ti:sapphire laser, emitting a smooth spectrum of 260-nm optical bandwidth, at full width at half maximum (FWHM), centered at 800-nm (Fuji et al., 2003). For retinal imaging, an alternate 110-MHz pulsed laser source, emitting a spectrum of 130-nm FWHM centered at 800-nm was used (Unterhuber et al., 2003). These Kerr-lens mode-locked lasers emit smooth ultra-broad spectra in the NIR (centered at 800-nm) directly out of a compact, prism-less and user-friendly oscillator with high power and high optical quality. The light emitted by the ultra-broad bandwidth pulsed laser source was distributed by fiber coupler BS1, with a splitting ratio of 90/10, to both the AO system and the interferometer, respectively. The interferometer consisted of a reference arm, a sample arm and the detector. The sample arm incorporated the AO system, which will be described in detail together with its operation later in this section. In the reference arm, the required amount of material for matching the chromatic dispersion produced by the AO system and the eye was introduced. The polarization of light in both arms was optimized, by using polarization controllers (PC), to maximize the interference signal at the detector. Linear polarization parallel to the initial orientation of the molecules in the PPM should be first generated in the sample arm. Then, the polarization in the reference arm should be adjusted till the same state of polarization than in the sample arm is achieved. A reflective diffraction grating based spectrometer (provided by Carl Zeiss Meditec, Dublin, CA) optimized for 130-nm bandwidth at 800-nm central wavelength was used as the detector. The spectrum was finally recorded on a linear 12-bit CCD camera with 2048 pixels (Atmel Aviva M2), placed behind the diffraction grating. The OCT system enabled up to 25,000 A-scan/s, permitting 3-D imaging of the living retina with a sensitivity of about 90-dB in the AO UHR OCT version used in the present study (Schmidt-Erfurth et al., 2005).

The AO system, presented in Fig. 2, was responsible of the measurement and the correction of ocular aberrations by means of a Hartmann-Shack wavefront sensor and the PPM, respectively. The AO setup incorporated a motorized optometer, described elsewhere (Fernández et al., 2001), for correcting the defocus independently of the rest of the AO system. Essentially, the optometer consists of a telescope with the capability for changing the distance between the two lenses (L1, $f'_{L1} = 200$ mm; L2, $f'_{L2} = 125$ mm) while keeping the position of these lenses fixed. This effect is achieved by movement of two pairs of plane mirrors mounted on a motorized stage, as it is shown in Fig. 2. The dynamic range for defocus correction–induction of the motorized optometer was ± 3.75-D. It has to be noted, that the optical path is changed, which requires simultaneous adjustment of the reference arm length.

The exit pupil of the eye was optically conjugated with the two scanning galvanometric mirrors (through L1 and L2, Y-scanning mirror; L3 and L4, $f'_{L3-4} = 150$ mm, X-scanning mirror); the correcting device (L5, $f'_{L5} = 50$ mm; SM1, $f'_{SM1} = 200$ mm); the wavefront sensor (SM1, $f'_{SM2} = 250$ mm; L6, $f'_{L6} = 60$ mm), and the diaphragm P1 placed in front of the collimator interfacing the AO system to the interferometer via optical fibers, labeled in the figure as C2. This diaphragm physically limits the pupil size

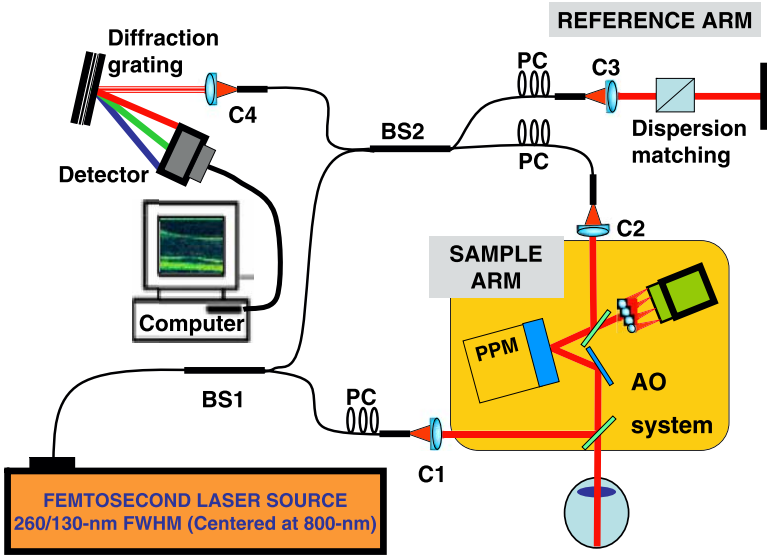

Fig. 1. Experimental apparatus. The frequency-domain interferometer incorporates the adaptive optics system in the sample arm, performing the aberration correction before the acquisition of the retinal images. An ultra-broad bandwidth laser source, emitting a smooth Gaussian spectrum, is used for retinal illumination.

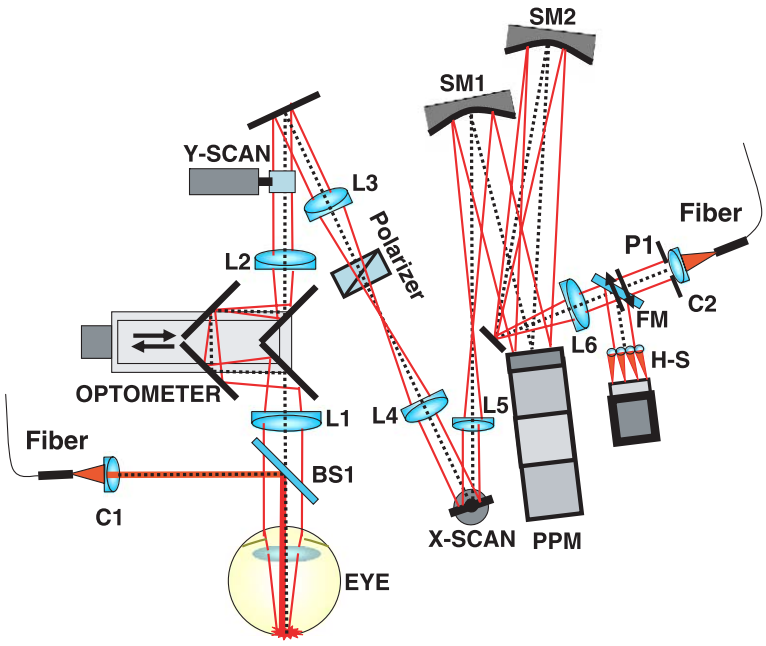

Fig. 2. Schematic of the adaptive optics system. The eye's exit pupil is optically conjugated on the two scanning mirrors, the PPM, the H-S wavefront sensor, and the collimator that connects the system to the interferometer, C2. The system incorporates a motorized optometer for correcting the defocus independently of the PPM.

on the subject's eye. The different planes in the AO system were conjugated by combining spherical mirrors (SM1, SM2) and achromatic doublet lenses specifically designed for the near IR (labeled in the figure as Li), optimizing the optical quality and reducing losses due to back-reflections in this portion of the spectrum. The use of spherical mirrors totally eliminates unwanted back-reflections, also making the setup more compact. However, the mandatory off-axis use of the spherical mirrors introduces some additional aberrations in the system, primary astigmatism, and spherical aberration, which can be compensated during the aberration correction. The main source of losses in the system was produced by the PPM. According to the technical specifications of the device, up to 15% of the incident light at 800-nm were absorbed.

The Hartmann-Shack wavefront sensor was compounded by an array of square microlenses mounted on a CCD camera, whose quantum efficiency was specifically optimized for the NIR range (Hamamatsu C7555). The size of each lenslet was 0.3-mm, with a focal length of 7.6-mm. The small size of the microlenses permitted a high spatial sampling of the wavefront, producing an accurate estimation of the incoming wave aberration. The aberrations were continuously obtained at 15-Hz, by measurement of the local slope of the wavefront (Prieto, Vargas-Martín, Goelz, & Artal, 2000).

2.1. Calibration of the correcting device

The PPM internally converts the intensity images sent from the computer into spatially modulated optical phase, as in the previous section has been described. The different gray levels of the projected images correspond to different optical paths introduced locally over the incoming wavefront. Therefore, different phase profiles can be induced by the PPM by using phase wrapping at a certain wavelength, in this case the central wavelength of the source spectrum, to represent the required wavefront. It is required to know the correspondence between gray levels and resulting changes in optical phase. To calibrate the device, the procedure described in the reference Prieto et al. (2004) was followed. During the first stage of the calibration different flat images were generated on the device with different gray levels, from 0 (black) to 255 (white), in steps of 20 intensity levels. Employing two polarizers, with their principal axis perpendicular to each other, both forming 45° with the initial orientation of the molecules of the PPM the phase response is translated into an intensity image. This was measured with the CCD camera coupled to the H-S sensor. The procedure inherently performed spatial average on the intensity through each of the microlenses (0.3-mm square) smoothing the effects of possible inhomogeneities in the liquid crystal layer. Once the flat images were recorded, a sinusoidal fit was performed of the intensity generated on the PPM as a function of the programmed gray level. This fit produced the required proportionality constant, or gain, between gray levels and generated phases. The PPM was calibrated once it was implemented in the AO system by using the ultra-broad bandwidth laser source. Fig. 3 shows the experimental values obtained for the phase gain at five different wavelengths from 700 to 900-nm, selected by using interference filters of 10-nm transmission bandwidth. The solid line depicts the gray level 255, as the maximum value available. The point

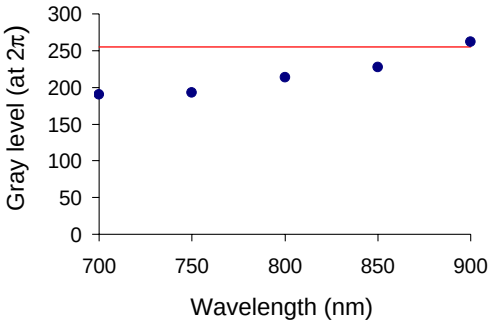

Fig. 3. Calibration of the correcting device. The points show the estimated gray levels for changes of 2π in optical phase, as a function of wavelength. The solid line corresponds to the maximum value of gray level, 255.

corresponding to 900-nm lays above this threshold, meaning that the device cannot exactly accomplish a full 2π phase shift for this wavelength at a given intensity, but could do so slightly below this value. For this particular device the maximum wavelength suitable for the induction of up to 2π phase changes was 880-nm. The range of wavelengths for 2π phase changes can be customized in the fabrication process of the PPM. In the following section, the effects of phase wrapping on a particular wavelength when using polychromatic light will be analyzed.

2.2. Aberration generation with polychromatic light

A fundamental difference of OCT as compared to other imaging techniques is the mandatory use of polychromatic light. The PPM cannot accomplish perfect aberration correction at different wavelengths simultaneously due to the inherent use of phase wrapping at a given selected wavelength. To evaluate the correction error of the PPM introduced by polychromatic light, we generated a known phase profile with the PPM at 800-nm, measuring the induced wavefront at different wavelengths as well as the corresponding point spread functions (PSFs) of the system. The wavefront was estimated by using the H-S sensor in a pupil of 6-mm diameter, while the PSFs were recorded by an auxiliary CCD camera located in place of the collimator that connects the AO system with the interferometer (see Fig. 2). To generate the PSF an achromatic doublet lens of 150-mm focal length in front of the auxiliary camera was used.

The different wavelengths were selected by using appropriate interference filter of 10-nm transmission bandwidth. The chromatic aberration introduced by the different elements compounding the system was initially measured. Its value remained close to the sensitivity of the H-S wavefront sensor; consequently it was not taken into account. Fig. 4 also includes a measurement of the aberrations when using the entire spectrum of the source. The intensity for the PSFs was controlled by adjusting the output from the pulsed laser, optimizing the signal in the auxiliary camera to avoid saturation. The signal in respect to the 900-nm PSF was rather weak, due to both the low emitted power from the laser source and the low sensitivity of the CCD at this particular wavelength. To improve visualization of the image, the contrast was altered in this case. Fig. 4 shows a significant agreement among the different wavefronts. The values of the total RMS of the measured aberrations were 0.89, 0.91, 0.99, 1.07, and 1.14-μm at 700, 750, 800, 850, and 900-nm, respectively. The difference of the values of the RMS between 750 and 800-nm, the range of interest, was 15%. Other aberrations were also induced

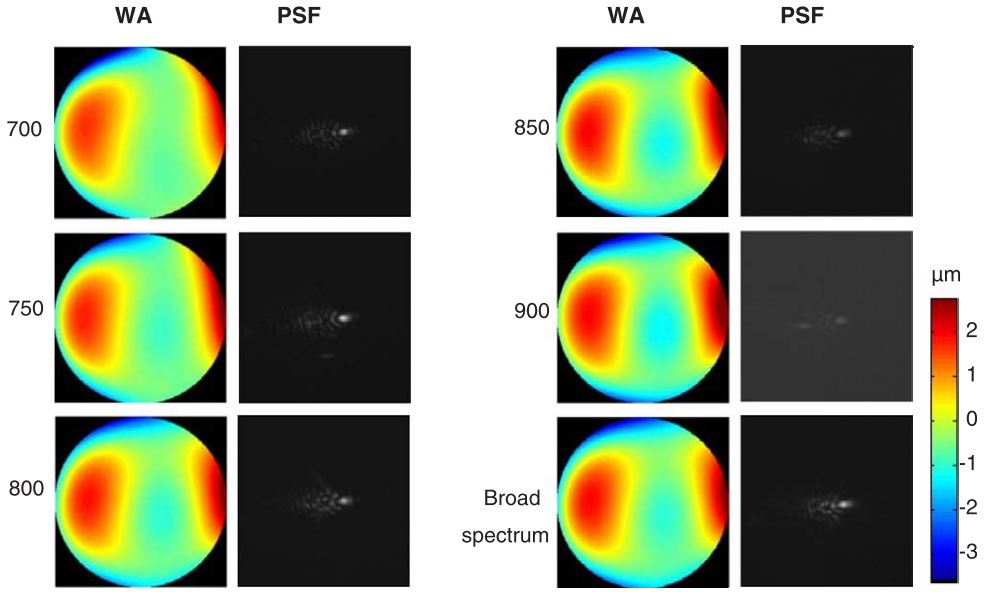

Fig. 4. Wavefront generated with the PPM at different wavelengths in a color-coded representation. The experimental PSFs, recorded with an auxiliary camera, are also shown. The different wavelengths were selected by using interference filter of 10-nm bandwidth. Due to the low emitted power of the source at 900-nm, and the low sensitivity of the CCD at this particular wavelength, the contrast and brightness of the PSF in this case were altered to permit a better visualization of the structure in the image.

on the PPM, performing a similar analysis, with comparable results. Regarding the shape of the PSF at different wavelengths, Fig. 4 exhibits a clear similarity among them, although an analysis in this case is more complex compared to the measurement of the wavefronts. These results indicate the feasibility of the use of the PPM as aberration corrector with polychromatic light sources. It should be noticed that the spectral distribution of energy used in UHR OCT for retinal imaging, the practical case in this work, is not flat, but Gaussian-shaped (130-nm FWHM). This means that the relative weight of the different wavelengths notably decreases with increasing offset from the central wavelength, in this case 800-nm. Consequently, the potential degradation of the retinal image produced by aberrations introduced by the wavelengths situated in the tails of the spectrum, and therefore their possible correction, is not as important as the ones placed in the surroundings of the central wavelength.

2.3. Closed-loop aberration correction

The capabilities and performance of the AO apparatus were tested by introducing static aberrations into the system. A dioptric telescope expanded the illumination beam at the entrance pupil of the system, allowing the generation of different aberrations by misaligning and tilting the two lenses. The telescope was located close to the collimator labeled in Fig. 2 as C1. A plane mirror was used behind BS1, allowing the light to enter into the AO system. An interference filter centered at 800-nm, 10-nm bandwidth, selected the central wavelength of the available spectrum. Fig. 5 shows the results of aberration correction performed by the PPM in a 6-mm pupil. The defocus was initially compensated by using the motorized optometer, leaving the rest of the aberrations to be corrected by the PPM. The initial aberration, practically free of defocus, presented a distortion peak-valley of more than 14 wavelengths at 800-nm. The iterative procedure for correcting the aberrations first consisted of the measurement of the incoming wavefront, for the subsequent generation of the opposite wavefront by the PPM. The combination of the external aberrations and the aberrations generated by the PPM were measured again, and additional corrections were superimposed until a corrected wavefront was obtained. To improve the convergence to the final corrected wavefront, it is required to introduce an attenuation factor to weigh the wavefront changes. This factor reduces the amplitude of the wavefront changes on the PPM, thereby increasing the number of required steps to achieve the desired surface. Gains near one generate a rapid correction, but stability is compromised, while on the contrary, gains close to zero augment the number of iterations to reach the final correction, but the stability is very high. The value we used along the measurements as a compromise between stability and number of iterations was 0.3. The gain factor also accounts for the slower temporal response of the correcting device (10–5 Hz) compared to the refreshing frequency ratio of the closed-loop operation (15 Hz). The system achieves an effective closed-loop bandwidth of 3 Hz.

Fig. 5 shows the evolution of the RMS of the wavefront as a function of time during the aberration correction in an artificial eye. In 0.5-s the correction achieved 80% of the perfect case, while in 2-s the correction was 92%. The final wavefront after correction was virtually free of aberrations, achieving the diffraction limit at 800-nm. The figure also includes the aberration maps, including the phase wrapping internally performed in the process, before and during the closed-loop aberration correction. The associated PSF, calculated from the measured wavefront, are also shown together with their corresponding Strehl's values. The example presented in this section demonstrates the capability of the PPM for near to perfect correction of highly aberrated wavefronts.

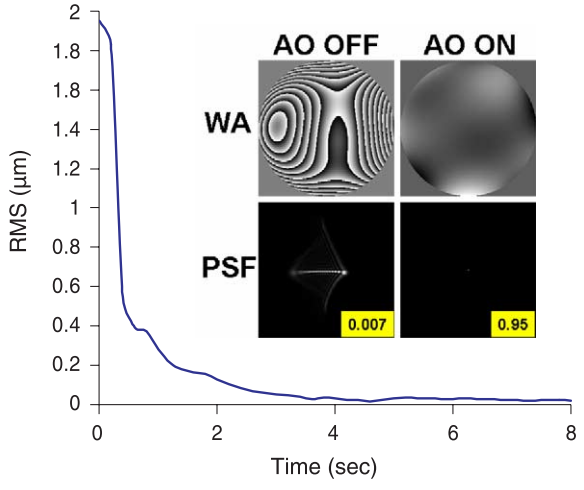

Fig. 5. Temporal evolution of the RMS during the closed-loop aberration correction in an artificial eye with 14 wave lengths peak-valley distortion. The wavefronts and their associated PSF, together with the Strehl ratio, before and during the correction are presented.

2.4. Effects of the phase wrapping on axial resolution

The large stroke of the PPM compared to other correcting devices originates in its ability to represent the programmed wavefront by phase wrapping. As it has been already discussed in previous sections, different wavelengths would require different phase wrappings, meaning that perfect aberration correction can only be exactly accomplished at a single wavelength, although the differences within the range of interest have been demonstrated to be quite small. There is however another effect, which might affect the axial resolution of the OCT tomograms. The fact that the phase variations introduced by the PPM are wavelength-dependent could distort the relative phase distribution among the different components of the spectrum. The phase jumps induced by the phase wrapping process do not affect the selected wavelength for which the whole setup is calibrated, due to the cyclic symmetry after a 2π revolution. For all the other wavelengths, but those

exactly one or multiple octaves away, the sudden jump in the phase introduces a slight phase mismatch that is proportional to the relative wavelength difference. Additionally, the lack of physical stroke, like in a Fresnel lens, does not shift the light pulse of a high stroke region back to the position of zero stroke. Therefore, a pulse that is continuously distorted and is smeared out in time by optical aberrations across the pupil will be chopped into small pulses that are corrected in their propagation direction, but are separated in time by a full oscillation period. While not significant for standard imaging, where time of flight does not play a role and in low resolution OCT with 30 and more oscillation per signal peak, this effect has the potential to compromise the axial resolution of an ultrahigh-resolution OCT system, which can achieve 5–10 oscillations per reflective site. Especially aberrations with high physical stroke would be affected. This could impair the axial resolution, which in low coherence interferometry is governed by the spectral shape of the light source. To evaluate this effect in practical application we recorded some retinal images with the AO system, while adding different aberrations with the PPM. Fig. 6 shows the retinal image measured by the system, 4.2 mm diameter at the eye's pupil, with the natural subject's aberrations, and the same image recorded after the addition of near 4-D of defocus with the PPM. As expected, the defocused image shows a clear decrease in the signal-to-noise ratio, induced by the dissipation of energy at the detector. However, the axial resolution in the tomogram remains practically unaffected.

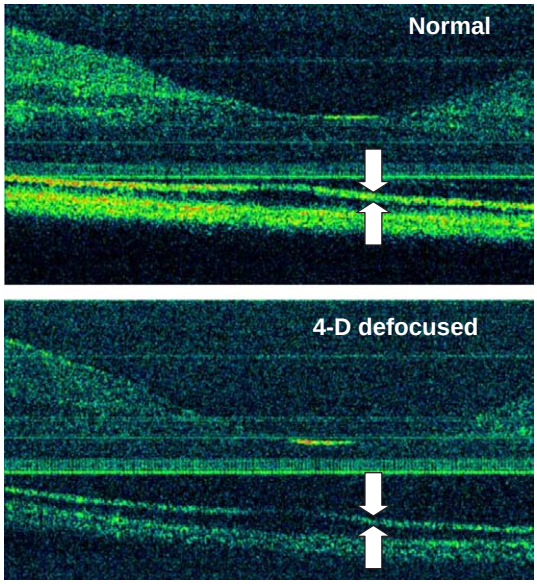

Fig. 6. Retinal OCT images obtained in the normal case and with 4-D of defocus introduced by the PPM. The inner–outer segment junction is marked by white arrows in both images. The edges of the different intraretinal layers are not degraded in the defocused case, indicating that phase wrapping performed by the PPM is not significantly affecting the axial resolution of the OCT images. The images also present some artifacts, in the form of horizontal straight lines, produced by back-reflections in the system. The appearance of these straight lines is also similar in both images.

The inner–outer segment junction, outlined in Fig. 6 by two arrows, can be resolved in both cases, showing no significant broadening in the defocused case. The edges of the retinal layers do not exhibit noticeable broadening or distortion in the defocused case compared to the normal case. Different aberrations were introduced by the PPM with similar results on the axial resolution of the retinal images, showing that the possible loss of axial resolution associated to the phase wrapping is negligible for common distortions.

2.5. Retinal imaging with AO UHR OCT

Once the PPM was tested, closed-loop aberration correction in the human eye could be accomplished. Retinal UHR OCT imaging was performed through the AO system with and without active aberration correction to study the benefits of this approach.

The left eye of two normal subjects (S1 and S2, aged 33 and 28, respectively), with no retinal pathology, were measured under paralyzed accommodation in a pupil of 6 mm. A bite-bar was used for positioning and stabilization of the subjects in the system. A 3-D stage held the subjects' dental impression, and a headrest fixated the forehead. The subjects' retinas were illuminated via the collimator C1, as it shown in Figs. 1 and 2. Once the subject was centered, the aberrations of the whole system, including the eye, were continuously measured by the H-S wavefront sensor. The defocus was first corrected by the motorized optometer. During the measurements, the flipping mirror (FP) allowed the light reflected by the subject's retina to reach the wavefront sensor, while blocking the light from the collimator that interfaced the interferometer. High order aberrations and remaining defocus were corrected by the PPM in closed-loop. Once the aberrations were corrected, the flip mirror FP position was moved and the light coming from the collimator H-S illumination was blocked. Thereafter, the subject's retina was illuminated from the collimator labeled in Figs. 1 and 2 as C2, enabling the interferometer to record the retinal images without aberrations. The retinal images were also recorded with the PPM deactivated, without correction of the ocular and system aberrations, except for the defocus, which remained corrected by the motorized optometer. Although, the ocular aberrations were measured with a pupil diameter of 6 mm, the effective pupil size used to obtain the retinal images was governed by the size of the diaphragm placed in front of the collimator C2, connecting the AO system to the interferometer, named in Fig. 2 as P1.

The effect of the aberration correction is presented in Fig. 7 for the two subjects. For each case, the left panel shows the initial aberrations and the associated PSF obtained at wavelength 800-nm. The right side corresponds to the average aberration measured after the closed-loop aberration correction. In both cases the final corrections achieved Strehl ratios above 0.7 in the selected pupil of 6-mm diameter at 800-nm Fig. 8.

To evaluate the effect of the aberration correction over the OCT images, some tomograms were acquired with

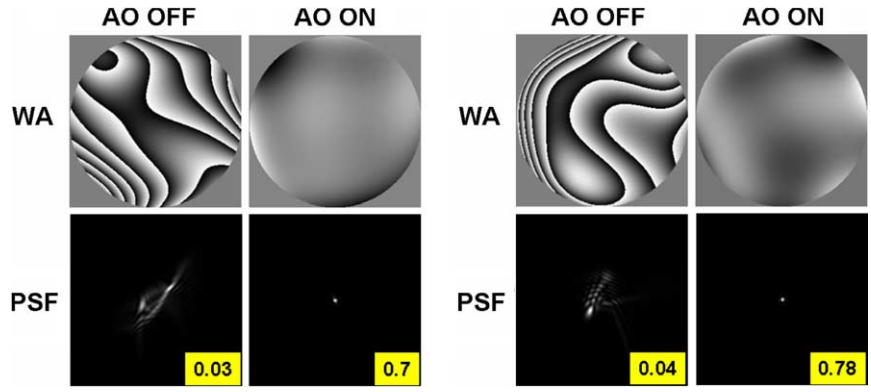

Fig. 7. Aberration maps, pupil size of 6-mm diameter, and associated PSFs before and during the closed-loop aberration correction performed in two subjects. The corresponding Strehl ratios are also shown on the PSFs.

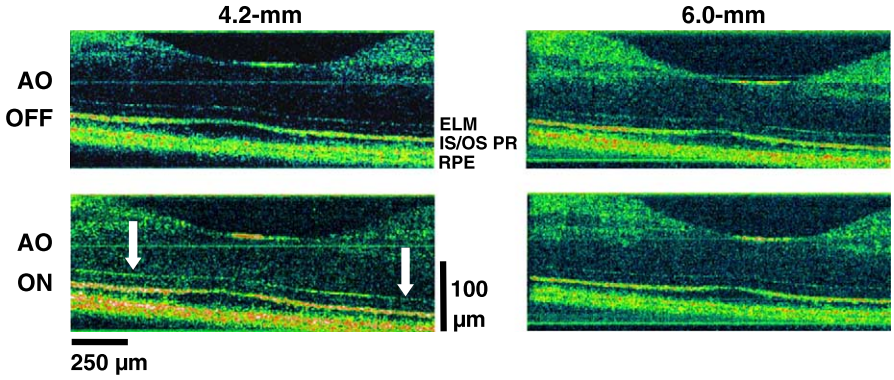

Fig. 8. Retinal OCT images obtained with and without AO through two different pupil sizes: 4.2 and 6-mm diameter.

and without using AO. The images were obtained through two different pupil sizes: 4.2- and 6-mm diameter, limited by P1. The aberrations were always measured and corrected in 6-mm diameter pupil. Fig. 9 presents two retinal images, corresponding to B-scans recorded with and without aberration correction from subject S1 using the two different pupil sizes. The images corresponding to 4.2-mm diameter covered approximately 1200-μm width, compounded by 850 A-scans, or equivalently a sampling ratio of 1.5-μm. The correction of the aberrations caused an increase in the signal-to-noise ratio, as the image at the bottom, left side, shows. This evident increase produces a clearer detection of some intraretinal structures, as the external limiting membrane (ELM). This particular layer is marked in the figure with two white arrows. Although, ELM is also visible in the uncorrected case, with aberrations, the image obtained without aberrations shows a stronger signal. The detected signal from the retinal pigmented epithelium (RPE) also incremented in the image recorded with AO. For this particular pupil diameter and this subject, the average increase in the signal-to-noise ratio produced by the aberration correction in the retinal images was 3dB.

Retinal images were also acquired using a 6-mm diameter pupil. The degradation of the retinal images due to the ocular aberrations should be larger in this case compared to the pupil of 4.2-mm and a stronger response to the correction was expected. Right panels in Fig. 9 present retinal images obtained of subject S1 in the foveal region, recorded with and without AO. The improvement of the image quality in the corrected case is not evident in this case. Surprisingly, no significant changes in the signal-to-noise of the OCT images obtained with AO through a pupil of 6-mm diameter were found. Therefore, different effects than the aberrations seem to play a role here.

Several factors affect the quality of the retinal images. In the case of low coherence interferometry techniques, the exigency of using polychromatic light introduces chromatic aberrations into the images. The ocular aberrations in the NIR have been studied in a previous work (Fernández et al., 2005). The chromatic defocus was evaluated in the range of interest for ophthalmic OCT, being around 0.22 D for a bandwidth of 130 nm FWHM centered at 800-nm. This chromatic aberration can be explained by using a simple water eye model. The optical performance of the experimental apparatus was modeled to evaluate the impact of the ocular chromatic aberration. It was found that the degradation of the signal at the detector, solely produced by the chromatic aberration, was strongly dependent on the pupil size for a given bandwidth. In particular, we found that for 4.2-mm of diameter the decrease of the detected signal due to the chromatic aberration respecting

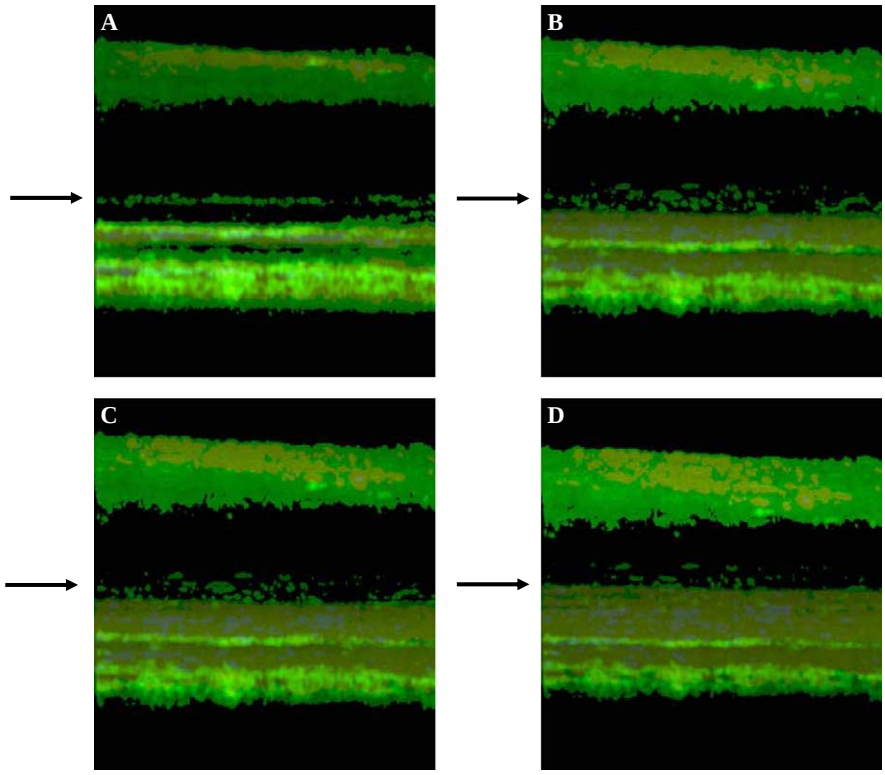

Fig. 9. Three-dimensional retinal volume of $750 \times 110 \times 400$-μm (transverse [$x$] × transverse [$y$]× axial [$z$]) about 1.3-mm nasally parafoveal at different angular perspectives; sample spacing of $0.73 \times 2.5 \times 0.75$-μm (transverse [$x$] × transverse [$y$] × axial [$z$]) resulting in $1024 \times 45 \times 550$ pixels. (A–D) depicts four different perspectives. Signals originating from the external limiting membrane (ELM, cf. black arrow) with 5–10-μm diameter might origin from groups of terminal bars (zonulae adherentes) that reflect more light as compared to the transparent rods and cones.

of the perfect case was less than 20%. However, for this particular bandwidth, the use of a pupil of 6-mm diameter produced loses of more than 60%. This high value could explain why the correction of the monochromatic aberration did not produce the expected benefit. In this case the impairment of the detected signal due to the chromatic aberration would be more important than the improvement due to the correction of monochromatic aberrations.

2.6. 3-D imaging with AO UHR OCT

Volumetric, 3-D representation of the living retina was obtained in a normal subject to study the benefits of AO through a pupil size of 4.2-mm diameter. Movie A shows the imaged retinal volume of $750 \times 110 \times 400$-μm (transverse [$x$]$x$ transverse [y] x axial [z]) about 1.3-mm nasally parafoveal at different angular perspectives. Sample spacing of $0.73 \times 2.5 \times 0.75$-μm (transverse [$x$] x transverse [y] x axial [z]) has been used resulting in $1024 \times 45 \times 550$ pixels. The whole retinal volume, equivalent to more than 25 Megavoxels was imaged within 2–4 s, depending on the used A-scan rate (10,000–25,000 A-scans/s). Fig. 9 depicts four different perspectives extracted from this movie. In Fig. 9A the perspective is normal to the retinal cross-section, i.e., a summation of all 45 B-scans across a 110-μm transverse [y] region, similar to the orientation of a histological section. In this view the signals originating from the external limiting membrane (ELM, cf. black arrow) appear as one diffuse, intersected line. In the other perspectives (cf. Fig. 9B–D) the 3-D appearance of this region can be appreciated better. The ELM is not a true membrane, but rather the attachment site between distal Müller cell processes unsheathing the photoreceptors at the transitory zone between outer nuclear layer and inner segments. These collar shaped contact zones are terminal bars (zonulae adherentes) that lack the zonula occludens portion. They represent the optically dense constituents of the ELM and might therefore reflect more light as compared to the transparent rods and cones (Fine & Yanoff, 1979). These signals, in the order of 5–10-μm size, might be caused by a group of neighboring rods where the surrounding terminal bars reflect light. These signals can be even more appreciated in Movie B, that depicts 500 reconstructed en face (C-mode scanning) UHR OCT images across a depth of 400-μm with 750×110-μm (transverse [x] x transverse [y]) imaged area and 0.7×2.5-μm (transverse [x] x transverse [y]) sample spacing. Fig. 10 depicts seven en face images, a zoom in of a region of 270×110-μm (transverse [x] x transverse [y]), covering a depth of 9-μm, starting in the outer nuclear layer and passing the ELM into the inner segment of the photoreceptors. The spacing between the different en face tomograms is indicated, arbitrarily starting with 0-μm. It is also obvious in Movie B and Fig. 9 that most of the signals do not seem to present speckle due to the reproducible

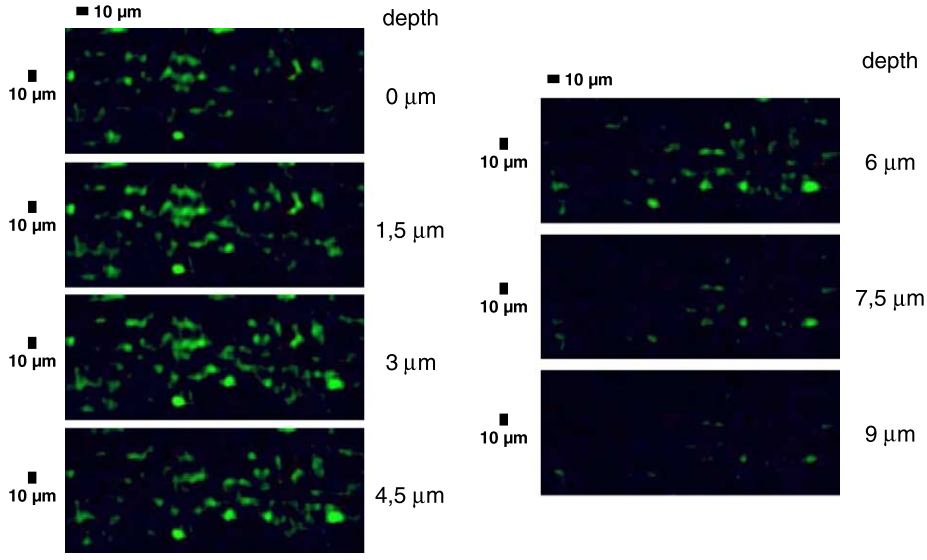

Fig. 10. Seven en face UHR OCT tomograms of 270 × 110-µm (transverse [x] × transverse [y]), covering a depth of 9-µm, starting in the outer nuclear layer and passing the ELM into the inner segment of the photoreceptors. The spacing between the different en face tomograms is indicated, arbitrarily starting with 0-µm.

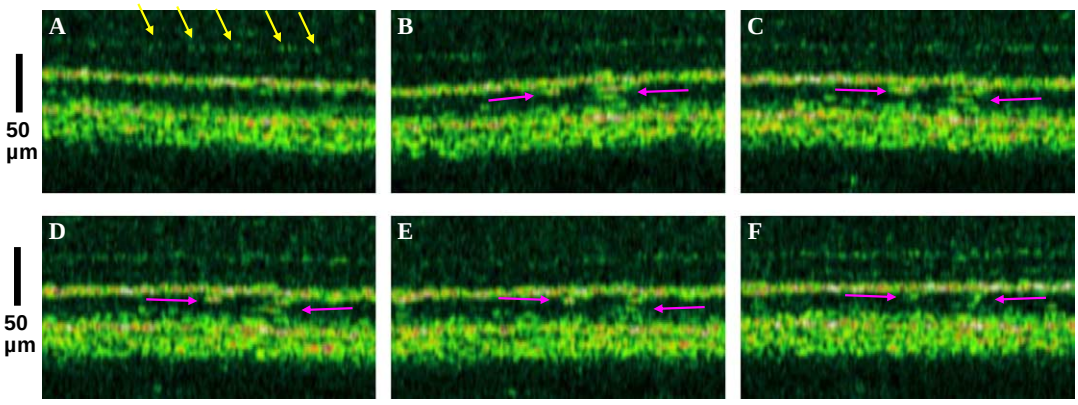

Fig. 11. Six representative B-scans with 2.5-µm transverse [y] spacing of 45 B-scans with 2.5-µm spacing (transverse [y]) across an area of 750 × 400-µm (transverse [x] × axial [z]) imaged with 0.73 × 0.75-µm (transverse [x] × axial [z]) sample spacing. In these B-scans (cf. yellow arrows, A) the ELM appears, similar as in light microscopy, as a discontinuous series of small dots originating from the terminal bars of groups of photoreceptors. In addition, morphological structures in the photoreceptor outer segment can clearly be visualized (cf. magenta arrows in (B–F).

visualization in adjacent en face images at different depths. Movie C shows a 'fly through' of all the 45 B-scans with 2.5-µm spacing (transverse [y]) across an area of 750 × 400-µm (transverse [x] x axial [z]) imaged with 0.73 × 0.75-µm (transverse [x] x axial [z]) sample spacing. Fig. 11 shows six representative B-scans with 2.5-µm transverse [y] spacing. In these B-scans (cf. yellow arrows, A) the ELM appears, similar as in light microscopy, as a discontinuous series of small dots originating form the terminal bars of the photoreceptors (Fine & Yanoff, 1979). In addition, morphological structures in the photoreceptor outer segment can clearly be visualized (cf. magenta arrows in Figs. 11B–F). Visualizing the 3-D structure of these features in five consecutive adjacent B-scans demonstrates that these appearances are unlikely speckles. Right now there are no clear anatomical explanations for this finding and further studies will clarify if these features might be very early indicators of morphological changes of the outer photoreceptor segments or the retinal pigment epithelium/Bruch's membrane/choriocapillaris interface.

3. Conclusions

In this manuscript a new application of the PPM for 3-D AO UHR OCT of the human retina has been presented. So far, this correcting device has been used in the eye in combination with monochromatic light sources (Prieto et al., 2004). OCT retinal imaging requires the use of broad bandwidth illumination, where the PPM has been tested. The performance of the spatial modulator with polychromatic light has been successfully demonstrated for aberration correction purposes in the living eye. The stroke of the

PPM, by performing phase wrapping, is widely superior to state-of-the-art deformable mirrors. Therefore, the PPM provides an interesting alternative for the accurate correction of low order aberrations: defocus and astigmatism. These terms are the most important ones in the human eye, in terms of their absolute contribution to the total aberration. Hence, the benefit of correcting high order aberrations is limited, unless perfect and accurate correction of defocus and astigmatism is accomplished. The situation in many ophthalmic AO systems is somehow paradox, since sophisticated methods are used to measure and correct for high order aberrations, whose contribution in normal and young eyes within moderate pupil sizes is known to be relatively modest, while defocus and astigmatism are still corrected by trial lenses placed in front of the eye.

The capability of the PPM to correct extreme aberration maps endowed with high spatial frequency patterns is also superior to any other correcting device, because of its huge number of independent pixels. It widely surpasses the requirements for correcting the aberrations in the normal human eye (Castejón-Mochón et al., 2002; Porter et al., 2001; Thibos et al., 2002), probably also being able to correct extreme aberrations found in pathologic cases, for instance in patients with transplanted corneas or those affected by keratoconus.

However, the response velocity in the PPM is significantly slower than in the case of regular deformable mirrors that accomplish frequencies in the kHz range. The maximum closed-loop aberration correction demonstrated with this device is around 4-Hz (Prieto et al., 2004). This value covers all the important dynamics found in the human eye (Hofer, Artal, Singer, Aragon, & Williams, 2001b), although benefits of using higher temporal bandwidths have been also demonstrated (Diaz-Santana, Torti, Munro, Gasson, & Dainty, 2003).

The benefits of aberration correction in the retinal images have been studied in a pupil size of 4.2-mm. An increase in the signal-to-noise ratio has been found, for better visualization of some intraretinal layers. This enhancement is of great practical interest for the use of automatic segmentation algorithms. The goal of these algorithms is the objective detection and measurement of the different intraretinal layers for the study and classification of the many different retinal conditions whose effects can degrade or alter the retinal morphology. The main obstacle when applying these algorithms is the weak signal received from some retinal layers, preventing their fully automatic operation in those cases. Therefore, the use of AO could notably increase the performance of automatic segmentation techniques.

In this work, we have measured the ocular aberrations by means of an H-S wavefront sensor. The light reflected by the retina has been analyzed in the sensor. It is known that for the NIR the most reflective layer is the RPE (Delori & Pflibsen, 1989). Therefore, the correction of the aberrations has been necessarily referred to this particular plane. Due to the use of a larger pupil size for imaging the retina, compared to the commonly used 1-mm of diameter pupil, the depth of focus is expected also to decrease accordingly. Therefore, the use of large pupils in combination with AO cannot produce a sharp image across the whole retinal thickness. The rigorous evaluation of both the transversal resolution and the depth of focus in OCT are of huge interest, and it should include the effects of chromatic aberration, monochromatic aberrations and the optical properties of the different retinal layers. Although, these calculations are beyond the scope of this work, we found that, as it is expected following the preceding discussion, the effect of AO was locally visible at some retinal layers while the appearance of the rest of the retina did not show significant changes, although even a decrease in the detected signal would be reasonable in this scenario. The benefits of AO can be extended over the whole retinal volume by performing an appropriate scanning in depth once the ocular aberrations have been corrected, varying the plane of focus.

Following a detailed analysis of the 3-D images obtained with AO UHR OCT using the PPM, interesting features could be visualized at the level of the retinal ELM. The location and size of these structures, in the range of the 5-μm transversally, may indicate that they are connected to the reflections of terminal bars from several photoreceptors, in this case rods, inner segments. The appearance of the ELM in Movie A and Fig. 9 (cf. arrow), showing features with 5–10-μm diameter, suggests the presence of discontinuities. Discontinuous signals have been reported for the foveal ELM (Krebs & Krebs, 1989) but their significance and frequency of occurrence is unclear. These signals might be caused by the clusters of rods interspersed between cones along foveal meridians. Consequently, they should disappear at the central region of the fovea. As the collars around cone inner segments widens with their increasing diameters, groups of small diameter rods with their surrounding terminal bars might induce inhomogeneities in light reflectance. Alternatively the patchiness of the ELM signal may represent the connection sites of a select group of single Müller cells each encircling a group of photoreceptors with collars of zonulae. The known weak reflectivity of the photoreceptors, practically transparent, makes their direct detection extremely difficult. The photoreceptors act as biological wave-guides, optimizing the transmission of the light parallel to their orientation (Roorda & Williams, 2002). The manifestations of this property of the photoreceptors in vision have been widely studied, grouped under the Stiles–Crawford effects (Enoch, 1963; Stiles & Crawford, 1933), although its repercussion in high resolution retinal imaging has not been systematically studied so far. The guiding effect of the photoreceptors could optimize the illumination of the highly reflective RPE, also favoring the transmission of the back-reflected light from the RPE interface parallel to the particular direction of the outer segment (Prieto, McLellan, & Burns, 2005). The combination of these effects could also explain the appearance of the observed structures. More systematic studies using AO in combination of UHR OCT will be re-

quired to clarify whether these newly detected morphological details at the ELM level and beyond follow consistent patterns across foveal profiles and what (inter-) cellular correlates they are representing.

Acknowledgments

We gratefully acknowledge the contributions of L. Schachinger, Vienna University of Medicine. Diego Ayala, Laboratorio de Optica, Universidad de Murcia, is acknowledged by his help with the software. We acknowledge Alexandre Tumlinson, University of Arizona, for his useful help on the dispersion compensation issues. This research was supported in part by Hamamatsu Inc. (Dr. Schleinkofer), FWF Y159-PAT, the Christian Doppler Society, FEMTOLASERS Produktions GmbH, Carl Zeiss Meditec AG; grants BFM2001-0391 and FIS2004-02153, "Ministerio de Educacion y Ciencia," Spain, and Acción Integrada España-Austria HU2002-0011.

Appendix A. Supplementary material

Supplementary data associated with this article can be found, in the online version, at doi:10.1016/j.visres.2005.08.028.

References

Castejón-Mochón, J. F., López-Gil, N., Benito, A., & Artal, P. (2002). Ocular wavefront aberration statistics in a normal young population. *Vision Research, 42*, 1611–1617.

Cense, B., Nassif, N., Chen, T., Pierce, M., Yun, S., Park, B., Bouma, B., Tearney, G., & de Boer, J. (2004). Ultrahigh resolution high-speed retinal imaging using spectral-domain optical coherence tomography. *Optics Express, 12*, 2435–2447, http://www.opticsexpress.org/abstract.cfm?URI=OPEX-12-11-2435.

Delori, F. C., & Pflibsen, K. P. (1989). Spectral reflectance of the human ocular fundus. *Applied Optics, 28*, 1061–1067.

Diaz-Santana, L., Torti, C., Munro, I., Gasson, P., & Dainty, C. (2003). Benefit of higher closed–loop bandwidths in ocular adaptive optics. *Optics Express, 11*, 2597–2605, http://www.opticsexpress.org/abstract.cfm?URI=OPEX-11-20-2597.

Drexler, W. (2004). Ultrahigh resolution optical coherence tomography. *Journal of Biomedical Optics, 9*, 47–74.

Drexler, W., Morgner, U., Ghanta, R. K., Kärtner, F. X., Schuman, J. S., & Fujimoto, J. G. (2001). Ultrahigh-resolution ophthalmic optical coherence tomography. *Nature Medicine, 7*, 502–507.

Drexler, W., Morgner, U., Kärtner, F. X., Pitris, C., Boppart, S. A., Li, X. D., Ippen, E. P., & Fujimoto, J. G. (1999). In vivo ultrahigh-resolution optical coherence tomography. *Optics Letters, 24*, 1221–1223.

Drexler, W., Sattmann, H., Hermann, B., Ko, T. H., Stur, M., Unterhuber, A., Scholda, C., Findl, O., Wirtitsch, M., Fujimoto, J. G., & Fercher, A. F. (2003). Enhanced visualization of macular pathology using ultrahigh resolution optical coherence tomography. *Archives of Ophthalmology, 121*, 695–706.

Enoch, J. M. (1963). Optical properties of the retinal receptors. *Journal of the Optical Society of America A, 53*, 71–85.

Fercher, A. F., Hitzenberger, C. K., Kamp, G., & El-Zaiat, S. Y. (1995). Measurement of intraocular distances by backscattering spectral interferometry. *Optics Communications, 117*, 43–48.

Fernández, E. J., & Artal, P. (2003). Membrane deformable mirror for adaptive optics: performance limits in visual optics. *Optics Express, 11*, 1056–1069, http://www.opticsexpress.org/abstract.cfm?URI=OPEX-11-9-1056.

Fernández, E. J., Iglesias, I., & Artal, P. (2001). Closed-loop adaptive optics in the human eye. *Optics Letters, 26*, 746–748.

Fernández, E. J., Unterhuber, A., Prieto, P. M., Hermann, B., Drexler, W., & Artal, P. (2005). Ocular aberrations as a function of wavelength in the near infrared measured with a femtosecond laser. *Optics Express, 13*, 400–409, http://www.opticsexpress.org/abstract.cfm?URI=OPEX-13-2-400.

Fine, B. S., & Yanoff, M. (1979). *Ocular Histology* (second ed.). Harper and Row Publishers Inc.

Fuji, T., Unterhuber, A., Yakovlev, V. S., Tempea, G., Stingl, A., Krausz, F., & Drexler, W. (2003). Generation of smooth ultra-broadband spectra directly from a prism-less Tisapphire laser. *Applied Physics B, 77*, 125–128.

Hermann, B., Fernández, E. J., Unterhuber, A., Sattmann, H., Fercher, A. F., Drexler, W., Prieto, P. M., & Artal, P. (2004). Adaptive optics ultrahigh resolution optical coherence tomography. *Optics Letters, 29*, 2142–2144.

Hofer, H., Artal, P., Singer, B., Aragon, J. L., & Williams, D. R. (2001b). Dynamics of the eye's wave aberration. *Journal of the Optical Society of America A, 18*, 497–506.

Hofer, H., Chen, L., Yoon, G. Y., Singer, B., Yamauchi, Y., & Williams, D. R. (2001a). Performance of the Rochester 2nd generation adaptive optics system for the eye. *Optics Express, 8*, 631–643, http://www.opticsexpress.org/abstract.cfm?URI=OPEX-8-11-631.

Huang, D., Swanson, E. A., Lin, C. P., Schuman, J. S., Stinson, W. G., Chang, W., Hee, M. R., Flotte, T., Gregory, K., Puliafito, C. A., & Fujimoto, J. G. (1991). Optical coherence tomography. *Science, 254*, 1178–1181.

Krebs, I. P., & Krebs, W. (1989). Discontinuities of the external limiting membrane in the fovea centralis of the primate retina. *Experimental Eye Research, 48*, 295–301.

Ko, T. H., Fujimoto, J. G., Duker, J. S., Paunescu, L. A., Drexler, W., Baumal, C. R., Puliafito, C. A., Reichel, E., Rogers, A. H., & Schuman, J. S. (2004). Comparison of ultrahigh and standard resolution optical coherence tomography for imaging macular hole pathology and repair. *Ophthalmology, 111*, 2033–2043.

Leitgeb, R., Drexler, W., Unterhuber, A., Hermann, B., Bajraszewski, T., Le, T., Stingl, A., & Fercher, A. (2004). Ultrahigh resolution Fourier domain optical coherence tomography. *Optics Express, 12*, 2156–2165, http://www.opticsexpress.org/abstract.cfm?URI=OPEX-12-10-2156.

Li, F. H., Mukohzaka, N., Yoshida, N., Igasaki, Y., Toyoda, H., Inoue, T., Kobayashi, Y., & Hara, T. (1998). Phase modulation characteristics analysis of optically-addressed parallel-aligned nematic liquid crystal phase-only spatial light modulator combined with a liquid crystal display. *Optical Review, 5*, 174–178.

Miller, D.T., Qu, J., Jonnal, R.S., Thorn, K. (2003). Coherence gating and adaptive optics in the eye. In: Tuchin, V.V., Izatt, J.A., Fujimoto, J.G. (Eds.), *Coherence Domain Optical Methods and Optical Coherence Tomography in Biomedicine VII, Proc. SPIE 4956*, 65–72.

Porter, J., Guirao, A., Cox, I. G., & Williams, D. R. (2001). Monochromatic aberrations of the human eye in a large population. *Journal of the Optical Society of America A, 18*, 1793–1803.

Prieto, P. M., Fernández, E. J., Manzanera, S., & Artal, P. (2004). Adaptive optics with a programmable phase modulator: applications in the human eye. *Optics Express, 12*, 4059–4071, http://www.opticsexpress.org/abstract.cfm?URI=OPEX-12-17-4059.

Prieto, P. M., McLellan, J. S., & Burns, S. A. (2005). Investigating the light absorption in a single pass through the photoreceptor layer by means of the lipofuscin fluorescence. *Vision Research, 45*, 1957–1965.

Prieto, P. M., Vargas-Martín, F., Goelz, S., & Artal, P. (2000). Analysis of the performance of the Hartmann-Shack sensor in the human eye. *Journal of the Optical Society of America A, 17*, 1388–1398.

Roorda, A., Romero-Borja, F., Donnelly, W. J., III, Queener, H., Hebert, T. J., & Campbell, M. C. W. (2002). Adaptive optics scanning laser ophthalmoscopy. *Optics Express, 10*, 405–412, http://www.opticsexpress.org/abstract.cfm?URI=OPEX-10-9-405.

Roorda, A., & Williams, D. R. (2002). Optical fiber properties of individual human cones. *Journal of Vision, 2*, 404–412, http://journalofvision.org/2/5/4/.

Schmidt-Erfurth, U., Leitgeb, R., Michels, S., Považay, B., Sacu, S., Hermann, B., Ahlers, C., Sattmann, H., Scholda, C., Fercher, A. F., & Drexler, W. (2005). Three-dimensional ultrahigh resolution optical coherence tomography of macular pathologies. *Investigative Opthalmology and Visual Science, 46*, 3393–3402.

Stiles, W.S., Crawford, B.H. (1933). The luminous efficiency of rays entering the eye pupil at different points. Proceedings of the Royal Society of London. *Series B: Biological Sciences 112*, 428–450.

Swanson, E. A., Izatt, J. A., Hee, M. R., Huang, D., Lin, C. P., Schuman, J. S., Puliafito, C. A., & Fujimoto, J. G. (1993). In vivo retinal imaging by optical coherence tomography. *Optics Letters, 18*, 1864–1866.

Thibos, L. N., Hong, X., Bradley, A., & Cheng, X. (2002). Statistical variation of aberration structure and image quality in a normal population of healthy eyes. *Journal of the Optical Society of America A, 19*, 2329–2348.

Unterhuber, A., Považay, B., Hermann, B., Sattmann, H., Drexler, W., Yakovlev, V., Tempea, G., Schubert, C., Anger, E. M., Ahnelt, P. K., Stur, M., Morgan, J. E., Cowey, A., Jung, G., Le, T., & Stingl, A. (2003). Compact, low-cost $TiAl_2O_3$ laser for in vivo ultrahigh-resolution optical coherence tomography. *Optics Letters, 28*, 905–907.

Wojtkowski, M., Srinivasan, V., Ko, T., Fujimoto, J. G., Kowalczyk, A., & Duker, J. (2004). Ultrahigh-resolution, high speed Fourier-domain optical coherence tomography and methods for dispersion compensation. *Optics Express, 12*, 2404–2421, http://www.opticsexpress.org/abstract.cfm?URI=OPEX-12-11-2404.

Zhang, Y., Rha, J., Jonnal, R. S., & Miller, D. T. (2005). daptive optics spectral optical coherence tomography for imaging the living retina. *Optics Express, 13*, 4792–4811, http://www.opticsexpress.org/abstract.cfm?URI=OPEX-13-12-4792.